NETWORK ADJUSTMENT OF ORBIT ERRORS IN SAR INTERFEROMETRY

Hermann Bähr[1] and Ramon Hanssen[2]

[1]*Geodetic Institute, Karlsruhe Institute of Technology, Englerstrasse 7, 76131 Karlsruhe, Germany, baehr@kit.edu*
[2]*Department of Earth Observations and Space Systems, Delft University of Technology, Kluyverweg1, 2629 HS Delft, The Netherlands, R.F.Hanssen@tudelft.nl*

ABSTRACT

Orbit errors can induce significant long wavelength error signals in synthetic aperture radar (SAR) interferograms and thus bias estimates of wide-scale deformation phenomena. The presented approach aims for correcting orbit errors in a preprocessing step to deformation analysis by modifying state vectors. Whereas absolute errors in the orbital trajectory are negligible, the influence of relative errors (baseline errors) is parametrised by their parallel and perpendicular component as a linear function of time. As the sensitivity of the interferometric phase is only significant with respect to the perpendicular baseline and the rate of change of the parallel baseline, the algorithm focuses on estimating updates to these two parameters. This is achieved by a least squares approach, where the unwrapped residual interferometric phase is observed and atmospheric contributions are considered to be stochastic with constant mean. To enhance reliability, baseline errors are adjusted in an overdetermined network of interferograms, yielding individual orbit corrections per acquisition.

Key words: Synthetic Aperture Radar; Interferometry; Orbit Errors.

1. INTRODUCTION

In spaceborne repeat-pass synthetic aperture radar (SAR) interferometry, the interferometric phase is corrected for the effect of different orbit trajectories of the satellite during the two acquisitions, referred to as master and slave. This is achieved by subtracting the simulated phase contribution of the acquisition geometry, the reference phase, from the measured interferogram. The geometry is determined by both the satellite orbits and a digital elevation model (DEM) of the terrain. Assuming that a DEM is available, a distinction between contributions of the ellipsoid and the DEM is not required. If the orbit information is inaccurate, errors propagate into the reference phase, inducing a nearly linear "phase ramp" in the interferogram that superposes the desired information, e. g. surface displacements.

A common approach to account for orbit errors is to subtract an estimated linear spatial trend from the unwrapped interferometric phase. A more sophisticated approach has been proposed by Massonnet and Feigl [1]: It corrects the parallel baseline based on the fringe count along the edges of the interferogram but does not account for the change of the perpendicular baseline over range [2].

Kohlhase et al. [3] resolved this deficiency by formulating the relation between phase differences and errors in the orbital trajectories more rigorously, associating phase gradients in range with across-track errors and gradients in azimuth with radial errors. This approach requires that the orbital contribution dominates the error budget, since again the fringe counts along the edges of the interferogram serve as observations.

The approach presented in this contribution adopts the basic functional model from [3], involving further enhancements though. It relies on the unwrapped interferometric phases of pixels distributed all over the interferogram, thus enabling applicability even if no distinct fringes occur. Furthermore, correlations between across-track and radial error components are taken into account in a joint estimation. Finally, an overdetermined network of linearly dependent interferometric combinations is considered to enhance precision and reliability by adjustment of the estimated errors. The network approach has already been successfully applied by Biggs et al. [4], who adjusted linear phase ramps to the interferograms rather than modifying the orbit information though.

The algorithm is designed as a preprocessing step to interferometric analysis. It assumes that orbit errors are the only deterministic signal component in the residual interferometric phase, which is indeed a very rough simplification. Whereas the bias due to small-scale signals is limited, wide-scale deformation phenomena and lateral atmospheric pressure gradients may leak significantly into the orbit estimates. If the signal of interest is deformation, the bias due to the atmospheric delay can be accepted. A distinction with respect to the deformation could be achieved by a posteriori temporal filtering of the estimates.

After a general characterisation of orbit errors, the estimation model for baseline errors in individual interfero-
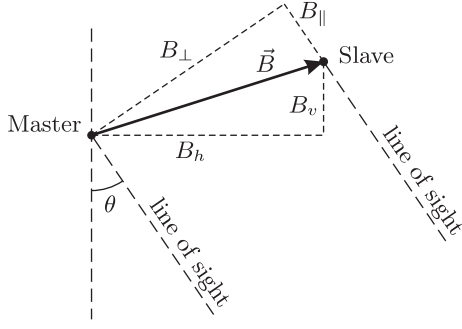
Figure 1. Decomposition of the interferometric baseline into horizontal/vertical (B_h/B_v) and parallel/perpendicular ($B_\parallel$/$B_\perp$) component, respectively.
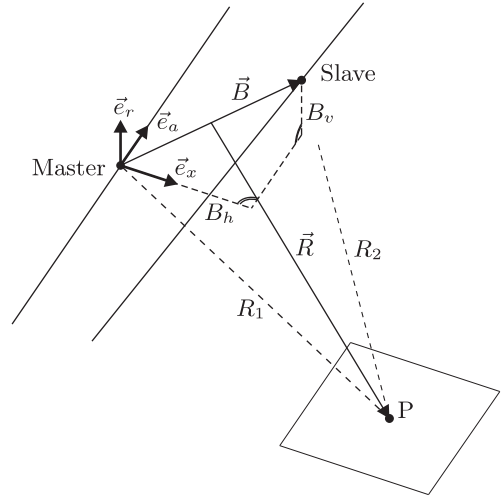

Figure 2. Definition of the baseline decomposition by the Frenet trihedron of the master's orbital trajectory, consisting of unit vectors in across-track ($\vec{e}_x$), along-track ($\vec{e}_a$) and radial ($\vec{e}_r$) direction.

grams will be derived. It will be shown how these estimates are adjusted in a network, which is demonstrated for some data acquired by the European Environmental Satellite (ENVISAT).

2. CHARACTERISATION OF ORBIT ERRORS

Whereas absolute orbit errors cancel out in the phase difference of two images, relative errors have a significant effect on the interferogram. Addressed are errors in the interferometric baseline $\vec{B}$, which is defined as the difference vector between the sensor positions during the acquisition of the same point on the surface (see fig. 1). Although this vector is three-dimensional, errors in the along-track component are are assumed to be sufficiently corrected for by coregistration [2]. Thus, the following considerations are restricted to the projection of the baseline onto a plane perpendicular to the track. Therein, it can be decomposed into a horizontal component B_h and a vertical component B_v. Depending on the look-angle θ, which is itself a function of range R, a different representation is the decomposition into parallel and perpendicular component [2]:

$$B_\parallel = B_h \cdot \sin\theta(R) - B_v \cdot \cos\theta(R)$$
$$B_\perp = B_h \cdot \cos\theta(R) + B_v \cdot \sin\theta(R) \ . \tag{1}$$

The reference phase at a point P on the surface is computed from the range difference of the two acquisitions and can be approximated using the parallel baseline component (see also fig. 2):

$$\phi = \frac{4\pi}{\lambda}(R_2 - R_1) \approx -\frac{4\pi}{\lambda}B_\parallel \ , \tag{2}$$

where λ is the radar wavelength (5.624 cm for ENVISAT) and t denotes the acquisition time. Hence, errors $dB_\parallel$ in the parallel baseline can cause errors $d\phi$ in the reference phase. The effect results as a first approximation in a constant phase shift. Since the interferometric phase is a relative measure, this does not influence the interpretation of

the interferogram though. Visible fringes are rather due to the spatial change of the interferometric phase. Differentiating eq. (2) with respect to $\theta(R)$ and t:

$$d\phi = -\frac{4\pi}{\lambda}\dot{B}_\parallel dt - \frac{4\pi}{\lambda}B_\perp d\theta \tag{3}$$

enables an assessment of the amount of baseline error that is equivalent to one fringe spanning the whole extent of the interferogram. With Δt = 16.3 s and $\Delta\theta$ = 6.2° it can be concluded that an error $d\dot{B}_\parallel = \lambda/(2\Delta t)$ = 1.7 mm/s causes one fringe in azimuth, whereas an error $dB_\perp = \lambda/(2\Delta\theta)$ = 26 cm is equivalent to one fringe in range. Fig. 3 shows the fringe patterns corresponding to specific baseline error components. They have been simulated rigorously without any approximation. Obviously, errors in both $\dot{B}_\parallel$ and $B_\perp$ induce a nearly linear fringe pattern in azimuth and range, respectively. The superposition of the two gives likewise linear patterns with a variable orientation of fringes, the well-known "phase ramps". In comparison, the influence of errors in $B_\parallel$ and $\dot{B}_\perp$ is marginal.

3. ESTIMATION OF BASELINE ERRORS

Reversing the considerations from the previous section, baseline errors can also be estimated from residual phase patterns in unwrapped interferograms. As the baseline is a relative measure, a distinction between errors in master and slave orbit cannot be made. To keep the derivation of the model most generic, an estimated error will be attributed in equal parts to both acquisitions. For the representation of the baseline, a decomposition into horizontal and vertical component has been chosen, since this does
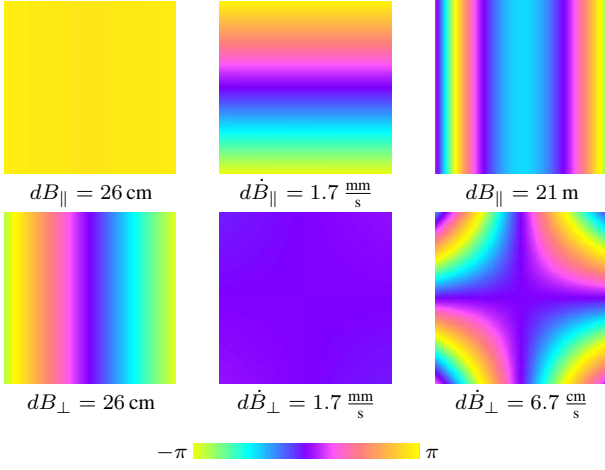
$dB_\parallel = 26\,\mathrm{cm}$ $d\dot{B}_\parallel = 1.7\,\frac{\mathrm{mm}}{\mathrm{s}}$ $dB_\parallel = 21\,\mathrm{m}$

$dB_\perp = 26\,\mathrm{cm}$ $d\dot{B}_\perp = 1.7\,\frac{\mathrm{mm}}{\mathrm{s}}$ $d\dot{B}_\perp = 6.7\,\frac{\mathrm{cm}}{\mathrm{s}}$

$-\pi$ ▬▬▬▬▬ π

Figure 3. Error signals induced into the interferometric phase by errors in different baseline components, where the decomposition into $B_\parallel$ and $B_\perp$ has been defined by the line of sight to the image centre. The two interferograms on the left show that the effect of an error in $B_\parallel$ is negligible compared to an error of the same amount in $B_\perp$. In the middle, an analogous conclusion can be drawn for $\dot{B}_\perp$ and $\dot{B}_\parallel$. On the right, the interferometric patterns related to errors in $B_\parallel$ and $\dot{B}_\perp$ are shown, requiring a disproportionately higher amount of error though.

not depend on range. It is defined by the Frenet trihedron of the master trajectory (see fig. 2). To account for the variation of the baseline error in azimuth, a linear time evolution is likewise estimated. Assuming that inaccurate orbits are the only systematic error source, the expectation of the unwrapped residual interferometric phase is:

$$\mathrm{E}\{\phi\} = \frac{4\pi}{\lambda}(R_2 - R_1) + \phi_0 , \qquad (4)$$

where ϕ_0 is a constant phase shift that accounts for the fact that the absolute range measurement is less precise than the phase measurement. Linearisation yields:

$$d\phi = \underbrace{-\frac{4\pi}{\lambda R}\,\vec{R}\vec{e}_x}_{=:a_h}\,dB_h - \underbrace{\frac{4\pi}{\lambda R}\,\vec{R}\vec{e}_r}_{=:a_v}\,dB_v + d\phi_0 , \quad (5)$$

where $\vec{R}$ is the range vector from the middle of the baseline to the surface point P (see fig. 2) and $R = |\vec{R}|$. For the estimation of baseline errors, multilooking is applied to reduce noise, and only the residual phases $d\phi_i$ ($i = 1 \ldots n_\phi$) of a well-distributed subset of sufficiently coherent pixels are considered. Estimation is performed in a Gauß-Markov Model [5]:

$$\mathrm{E}\{\mathbf{l}\} = \mathbf{A}\mathbf{x} , \qquad (6)$$

where $\mathbf{l}$ are the observations, $\mathbf{A}$ is the design matrix and $\mathbf{x}$ are the parameters of interest. The latter are baseline errors as a linear function of time. As ϕ_0 is only an auxiliary parameter without interest therein, it is eliminated from the model [6], yielding the following elements of eq. (6):

$$\mathbf{l} = \begin{pmatrix} \vdots \\ d\phi'_i \\ \vdots \end{pmatrix} , \qquad \mathbf{x} = \begin{pmatrix} dB_h \\ d\dot{B}_h \\ dB_v \\ d\dot{B}_v \end{pmatrix} ,$$

$$\mathbf{A} = \begin{pmatrix} \vdots & \vdots & \vdots & \vdots \\ a'_{h,i} & a'_{h,i}t_i & a'_{v,i} & a'_{v,i}t_i \\ \vdots & \vdots & \vdots & \vdots \end{pmatrix} , \qquad (7)$$

with $d\phi'_i = d\phi_i - d\bar{\phi}$, $a'_{h,i} = a_{h,i} - \bar{a}_h$ and $a'_{v,i} = a_{v,i} - \bar{a}_v$, where $d\bar{\phi}$, $\bar{a}_h$ and $\bar{a}_v$ are the arithmetic means of $d\phi_i$, $a_{h,i}$ and $a_{v,i}$, respectively, over all observations. For numerical purposes, the azimuth time t is normalised to the acquisition timespan of the master. The spatially homogeneous distribution of observed pixels over the whole extent of the interferogram is an essential postulation, since the estimates can be significantly biased by unbalanced configurations. Thus, the interferogram is divided into tiles, where only the pixel with the highest spatial coherence estimate is picked from each tile to contribute to the estimation.

Although it would seem reasonable to assign higher weights to pixels with higher coherence estimates, this has not been done to avoid leverage effects of locally clustered highly-weighted observations. Thus, an unweighted approach has been chosen for the stochastic model:

$$\mathrm{V}\{\mathbf{l}\} = \varsigma_0^2\mathbf{I} , \qquad (8)$$

where ς_0^2 is an a priori unknown variance factor. The baseline error estimates $\hat{\mathbf{x}}$ and their cofactor matrix $\mathbf{Q}_{\hat{x}\hat{x}}$ read:

$$\hat{\mathbf{x}} = (\mathbf{A}^T\mathbf{A})^{-1}\mathbf{A}^T\mathbf{l}$$
$$\mathbf{Q}_{\hat{x}\hat{x}} = (\mathbf{A}^T\mathbf{A})^{-1} . \qquad (9)$$

$\mathbf{Q}_{\hat{x}\hat{x}}$ contains information on the relative estimation quality of the baseline parameters. Whereas constant and linear components are uncorrelated for a balanced distribution of observations and a centred timescale, the correlations between horizontal and vertical components are significant and visualised qualitatively by error ellipses in fig. 4. The ellipses are severely elongated, and their main axes are aligned with the line of sight to the image centre. This orientation motivates the consideration of the decorrelated components $B_\parallel$ and $B_\perp$ rather than B_h and B_v.
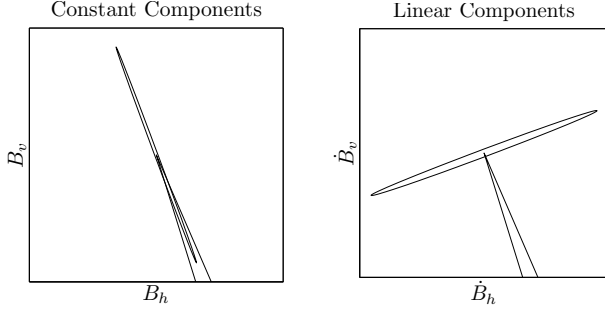
Figure 4. Relative estimation quality of constant and linear components of the baseline error, visualised by error ellipses. The radial lines mark the lines of sight to near and far range.

It follows from fig. 4 that $d\dot{B}_\parallel$ and $dB_\perp$ can be robustly estimated, whereas $dB_\parallel$ and $d\dot{B}_\perp$ are only weakly determined. This is coherent with the conclusion from the previous section, showing that a good estimation quality of a baseline component corresponds with a strong effect of errors in that component on the interferometric phase and vice versa.

Tests with real data have shown that the weakly determined parameters $dB_\parallel$ and $d\dot{B}_\perp$ are not reliably estimable due to their high sensitivity to small changes in the phase combined with the contribution of other, unmodelled signal components in the interferogram. However, as the influence on the interferometric phase is marginal (see fig. 3), it would not bias the result significantly to assume that the errors in these components are zero.

This assumption can be subsequently introduced into the estimation model, constraining the solution by $dB_\parallel(\theta) = 0$ and $d\dot{B}_\perp(\theta) = 0$ [5, pp. 170-177]. θ is defined here most generically by the orientation of the error ellipses, derived from the eigenspaces of $\mathbf{Q}_{\hat{x}\hat{x}}$. The constrained solution and its cofactor matrix read:

$$\hat{\mathbf{x}}_c = (\mathbf{I} - \mathbf{Q}_{\hat{x}\hat{x}}\mathbf{B}^T(\mathbf{B}\mathbf{Q}_{\hat{x}\hat{x}}\mathbf{B}^T)^{-1}\mathbf{B})\hat{\mathbf{x}}$$
$$\mathbf{Q}_{\hat{x}_c\hat{x}_c} = (\mathbf{I} - \mathbf{Q}_{\hat{x}\hat{x}}\mathbf{B}^T(\mathbf{B}\mathbf{Q}_{\hat{x}\hat{x}}\mathbf{B}^T)^{-1}\mathbf{B})\mathbf{Q}_{\hat{x}\hat{x}} \qquad (10)$$

with:

$$\mathbf{B} = \begin{pmatrix} \sin\theta & 0 & -\cos\theta & 0 \\ 0 & \cos\theta & 0 & \sin\theta \end{pmatrix} . \qquad (11)$$

$\hat{\mathbf{x}}_c$ contains baseline errors that are constrained to the $(d\dot{B}_\parallel, dB_\perp)$ solution-space, but represented by four parameters corresponding to B_h, $\dot{B}_h$, B_v and $\dot{B}_v$ though. This parameterisation is required for the application of corrections to the orbital trajectories before reprocessing the interferogram.

By estimation of the variance of unit weight:

$$\hat{\varsigma}_0^2 = \frac{(\mathbf{l} - \mathbf{A}\hat{\mathbf{x}}_c)^T(\mathbf{l} - \mathbf{A}\hat{\mathbf{x}}_c)}{n_\phi - 3} \qquad (12)$$

a covariance matrix of the constrained estimates $\hat{V}\{\hat{\mathbf{x}}_c\} = \hat{\mathbf{C}}_{\hat{x}_c\hat{x}_c} = \hat{\varsigma}_0^2\mathbf{Q}_{\hat{x}_c\hat{x}_c}$ can be obtained. It contains information on the absolute precision of the estimates and can be regarded as an indicator on how well an observed fringe pattern can be explained by orbit errors in $\dot{B}_\parallel$ and $B_\perp$. Due to rudimentary stochastic modelling, it is not considered to reflect the absolute level of precision realistically though.

4. NETWORK ADJUSTMENT

The estimation of baseline errors as described in the previous section can be performed for several interferograms in a set of images. If n_img images are available, $n_\text{img} - 1$ linearly independent interferograms can be formed, whereas $n_\text{img}(n_\text{img}-1)/2$ combinations would be possible. A standard procedure for a deformation analysis would be to select the $n_\text{img} - 1$ "best" combinations for processing of interferograms. However, the computation of more interferograms than necessary can be beneficial for the estimation of orbit errors. Due to geometric decorrelation, the information that is available from the images is not exploited completely by the formation of only $n_\text{img} - 1$ interferograms. Hence, the baseline error estimates between two images may vary slightly, depending on the linear combination of interferograms they have been derived from. Furthermore, the conditions for spatial unwrapping can be different. These effects are made use of to enhance precision and reliability of the estimates when processing more than $n_\text{img} - 1$ interferometric combinations.

The approach consists in setting up a network of "good" combinations and eliminating misclosures between baseline errors in a least squares adjustment. The choice of combinations is determined by the feasibility of unwrapping, requiring a good coherence. A small number of local unwrapping errors may be tolerated as long as the ambiguities are resolved correctly on a large scale. For consistency, it is necessary that the baseline estimates from the individual interferograms have a common reference in several respects:

- The (normalised) timescales t of all respective master acquisitions have to be homogenised within the whole set. To achieve this, the timescale of a unique set-master is adopted for all combinations.

- The moving coordinate frame $(\vec{e}_x, \vec{e}_r)$ that is required in eq. (5) must be likewise defined by a unique master orbit for the whole set.

- The decomposition of the baseline into parallel and perpendicular component that determines the constraints in eq. (11) must be uniform for the whole set. It is defined by a mean look angle θ, averaged over individual θ_i derived from eigenspaces of $\mathbf{Q}_{\hat{x}\hat{x},i}$ ($i = 1 \ldots n_{\mathrm{ifg}}$).

The adjustment is based on vectors of constrained baseline estimates $\hat{\mathbf{x}}_{c,i}$ and corresponding covariance matrices $\hat{\mathbf{C}}_{\hat{x}_c\hat{x}_c,i}$ for every interferogram – obtained by the method described in the previous section. As $\hat{\mathbf{x}}_{c,i}$ consists of four parameters with only two degrees of freedom, the baseline errors have to be transformed from the $(B_h, \dot{B}_h, B_v, \dot{B}_v)$- to the $(\dot{B}_\parallel, B_\perp)$-space beforehand:

$$\mathbf{y}_i = \mathbf{T}\hat{\mathbf{x}}_{c,i}$$
$$\mathbf{Q}_{yy,i} = \mathbf{T}\hat{\mathbf{C}}_{\hat{x}_c\hat{x}_c,i}\mathbf{T}^T \tag{13}$$

with:

$$\mathbf{T} = \begin{pmatrix} 0 & \sin\theta & 0 & -\cos\theta \\ \cos\theta & 0 & \sin\theta & 0 \end{pmatrix} , \tag{14}$$

where $\mathbf{y}_i$ are considered as observations in a subsequent adjustment step, and $\mathbf{Q}_{yy,i}$ are the associated cofactor matrices, defining the mutual weighting. Another Gauß-Markov Model is set up to adjust $2\,n_{\mathrm{img}}$ absolute orbit error parameters $\hat{\mathbf{z}}_j$ from the $2\,n_{\mathrm{ifg}}$ relative baseline error parameters $\hat{\mathbf{y}}_i$ ($i = 1 \ldots n_{\mathrm{ifg}}$, $j = 1 \ldots n_{\mathrm{img}}$). For interferogram k, formed between images l and m, the formulation of the model would be:

$$\mathrm{E}\{\mathbf{y}_k\} = \mathbf{z}_m - \mathbf{z}_l$$
$$\mathrm{V}\{\mathbf{y}_k\} = \sigma_0^2 \mathbf{Q}_{yy,k} , \tag{15}$$

where σ is again a global variance factor to be estimated a posteriori. As the problem is rank-deficient, the minimum-norm-solution is chosen, yielding best estimates in terms of precision. It can be obtained by conditioning the solution to fulfil [5, pp. 185-193]:

$$\sum_{j=1}^{n_{\mathrm{img}}} \hat{\mathbf{z}}_j = \mathbf{0} . \tag{16}$$

After transforming back the obtained estimates $\hat{\mathbf{z}}_j$ to the $(B_h, \dot{B}_h, B_v, \dot{B}_v)$-space, they can be used to correct the orbit trajectories before reprocessing the interferograms.

5. RESULTS

The approach has been applied on a set of 31 ENVISAT acquisitions from a scene in Western Australia (track 203,
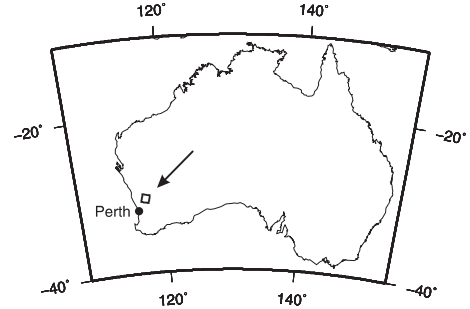

Figure 5. Location of ENVISAT track 203, frame 4421 on the Australian continent.

frame 4221), spanning more than four years from December 2003 until April 2008 (see fig. 5 and 6). The region has a semi-arid climate and is dominated by dryland cropping and some salt lakes, which involves a high coherence of interferograms and thus facilitates spatial unwrapping. The topography is relatively flat with height differences of less than 200 m.

The SAR data has been processed with the *Delft Object-Oriented Radar Interferometric Software* (DORIS – [7]), using precise orbits determined by the French *Centre National d'Etudes Spatiales* (CNES). The interferograms have been multilooked by factor 25 in azimuth and 5 in range. These factors have been found empirically, maximising coherence. The topographic effect in the reference phase has been accounted for using a 3"-DEM product from the *Shuttle Radar Topography Mission* (SRTM). For most interferograms, an adaptive phase filter [8] has been applied to facilitate unwrapping. The latter has been carried out using the *statistical-cost network-flow algorithm for phase unwrapping* (SNAPHU) [9]. To avoid a phase bias due to filtering, the unfiltered phase has been restored after unwrapping:

$$\phi_{\mathrm{restored}} = \phi_{\mathrm{unwrapped}} - \angle\, e^{i(\phi_{\mathrm{filtered}} - \phi_{\mathrm{unfiltered}})} , \tag{17}$$

assuming that the difference between filtered and unfiltered phase is small. This should hold at least for the highly coherent pixels that are used for the estimation of orbit errors. The coherence has been estimated spatially with a window size of 25×5 pixels.

The network consists of 162 combinations of interferograms, for which the unwrapping was sufficiently reliable (see fig. 7). The interferograms have been subdivided into tiles of 30×30 multilooked pixels, selecting the most coherent pixel from each tile to contribute to the estimation. Only a limited number of tiles with lack of pixels above a coherence threshold of 0.25 have not been considered. Based on the selected pixels, baseline errors up to $d\dot{B}_\parallel$ = 3.9 mm/s (12281-15287) and $dB_\perp$ = 80 cm (09275-10277) have been observed (see fig. 6 and tab. 1).

The network adjustment yielded estimates for orbit errors up to 2.8 mm/s in the $\dot{B}_\parallel$- and 66 cm in the $B_\perp$-component (both for 12281). Otten and Dow [10] esti-
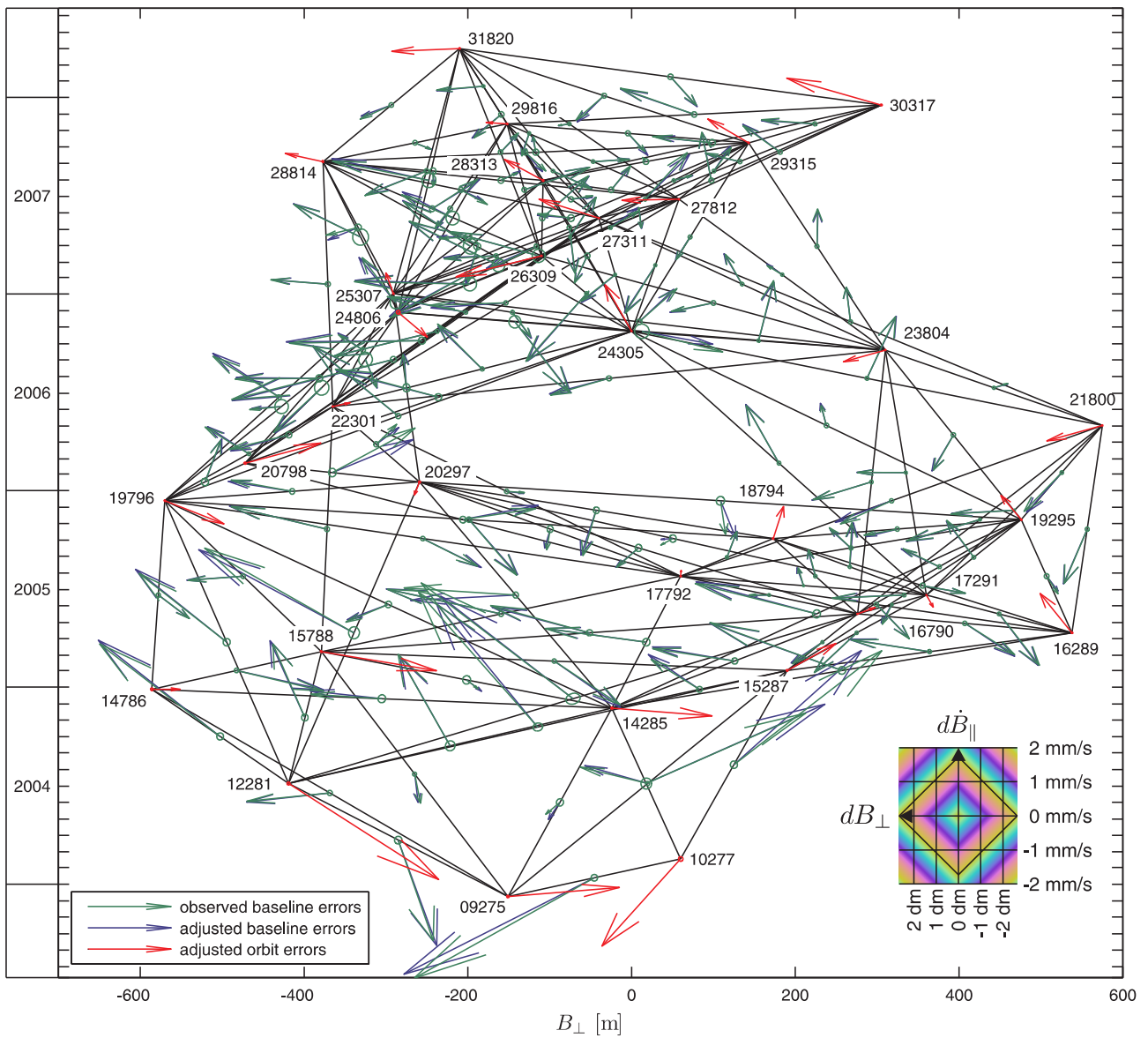
Figure 6. Network of interferometric combinations that has been used for the estimation of orbit errors. Vertices represent images (acquisitions with indicated orbit numbers), and edges stand for interferograms. The baseline errors that have been observed from the interferograms individually are denoted by green arrows. These visualise magnitude and orientation of the fringe gradient, where the number of orbital fringes in the interferogram can be obtained using the legend in the lower right corner. The conversion is based on the relation that one fringe in azimuth is equivalent to a baseline error of $d\dot{B}_{\parallel}$ = 1.7 mm/s and one fringe in range corresponds to $dB_{\perp}$ = 26 cm (cf. section 2). The adjusted orbit errors are visualised absolutely (per acquisition) by red arrows and relatively (per interferogram) by blue arrows. Hence, the deviation between green and blue arrows point out the misclosures of the network. Green (and very small red) error ellipses indicate the model precision, estimated from misclosures.
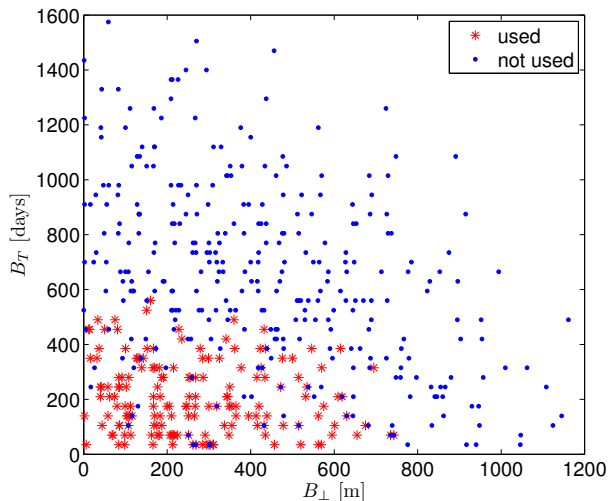
Figure 7. 162 of the 465 possible interferometric combinations have been used in the network. Most interferograms with a temporal baseline B_T above 500 days and a perpendicular baseline $B_\perp$ above 700 m could not be reliably unwrapped.

Table 1. Statistics of estimated orbit errors (per acquisition), "observed" baseline errors (per interferogram) and residuals (per interferogram), given in metric units and by the equivalent number of fringes ("fr."), respectively. $\hat{\sigma}$ denotes the respective root mean squared standard deviation, estimated using the weighted sum of squared residuals.

		$d\dot{B}_\parallel$		$dB_\perp$	
		$[\frac{mm}{s}]$	[fr.]	[cm]	[fr.]
Estimates	RMS	0.88	0.52	27.3	1.05
	max.	2.77	1.63	66.2	2.55
	$\hat{\sigma}$	0.03	0.02	0.4	0.02
Observations	RMS	1.08	0.64	27.0	1.04
	max.	3.88	2.29	79.6	3.06
	$\hat{\sigma}$	0.22	0.13	3.2	0.12
Residuals	RMS	0.08	0.05	1.7	0.06
	max.	0.39	0.23	9.0	0.35
	$\hat{\sigma}$	0.20	0.12	3.0	0.11

mate the accuracy of ENVISAT orbit products to be 3 cm in radial direction and 10 cm in 3D, respectively. However, these indications are neither upper bounds for errors, nor do they rely on completely independent validation strategies. Hence, the order of magnitude of the orbit errors estimated here is not totally unrealistic, although other signal components like the atmospheric contribution very likely leak into the estimates.

A strong point of the network approach is its capability to identify large-scale unwrapping errors. As every estimated baseline error is validated by several other interferometric combinations, outliers could be clearly identified and rejected from the network beforehand. There are still discrepancies up to 0.4 mm/s and 9 cm though. They are not considered to be outliers, since the unwrapping appears to be reliable and the distribution of observed points over the interferograms seems homogeneous. Timing errors, which have not been accounted for, are suspected to be the most likely cause, which has to be further investigated though. Nevertheless, correcting orbit errors according to the obtained error estimates should already be a considerable improvement. With 0.02 fringes in both range and azimuth direction, the model precision of the estimates is definitely acceptable, probably not reflecting the physical accuracy though.

Having processed 162 interferograms implies a huge computational load, considering that there are not more than 30 linearly independent combinations. That has been possible due to the favourable conditions of the dry region involving high coherence. However, the number of required combinations to yield an adequate result is probably smaller.

6. CONCLUSIONS

The presented method can be used to significantly reduce the influence of orbit errors in SAR interferometry. It relies on the unwrapped interferometric phase of distinct, homogeneously distributed pixels and assumes errors in both the perpendicular baseline and the temporal derivative of the parallel baseline. These components have been identified to have the most significant impact on the interferometric phase. The algorithm does not assume a linear error signal but rather models the functional relations rigorously. Adjusting estimated corrections in a network allows for enhancement of both precision and robustness with respect to outliers, eventually caused by unwrapping errors. A model precision of 0.02 fringes in both azimuth and range direction could be achieved. It is not required to coregister all images to a unique stack master, since the mutual reference between images is established via the orbits.

Unfortunately, the algorithm relies on spatial unwrapping, which turns out to be the limiting factor for the suitability of interferometric combinations. For many datasets, a direct application will be impossible due to lack of unwrapable combinations. However, there is

believed to be some potential in unwrapping strategies based on a sparse grid of coherent pixels. An iteration-based integration into a processing chain of persistent scatterer analysis seems likewise considerable. A clear drawback is the computational load that is associated with the processing of an extensive number of interferometric combinations.

Nevertheless, there is prospect of further enhancements. The influence of timing errors needs to be analysed in more detail. Refining the still rudimentary stochastic model could enable more sophisticated quality control. Finally, potential and methodology of distinction between orbital error signals and temporally correlated deformation signals still needs to be evaluated.

REFERENCES

[1] Massonnet, D. & Feigl, K. L. (1998). Radar interferometry and its Application to Changes in the Earth's Surface. *Reviews of Geophysics* 36(4), 441-500.

[2] Hanssen, R. F. (2001). *Radar Interferometry: Data Interpretation and Error Analysis*. Kluwer Academic Publishers, Dordrecht, The Netherlands.

[3] Kohlhase, A. O., Feigl, K. L. & Massonnet, D. (2003). Applying differential InSAR to orbital dynamics: a new approach for estimating ERS trajectories. *Journal of Geodesy* 77(9), 493-502.

[4] Biggs, J., Wright, T., Lu, Z. & Parsons, B. (2007). Multi-interferogram method for measuring interseismic deformation: Denali Fault, Alaska. *Geophysical Journal International* 170(3), 1165-1179.

[5] Koch, K. R. (1999). *Parameter Estimation and Hypothesis Testing in Linear Models*, 2nd ed. Springer, Berlin, Heidelberg, Germany.

[6] Jäger, R., Müller, T., Saler, H. & Schwäble, R. (2006). *Klassische und robuste Ausgleichungsverfahren*. Wichmann, Heidelberg, Germany, p. 37-38.

[7] Kampes, B. M., Hanssen, R. F. & Perski, Z. (2004). *Radar Interferometry with Public Domain Tools*. In Proc. FRINGE 2003 Workshop, Frascati, Italy, 1-5 Dec 2003, ESA-SP-550 (CD-ROM), ESA Publications Division, European Space Agency, Noordwijk, The Netherlands.

[8] Goldstein, R. M. & Werner, C. L. (1998). Radar interferogram filtering for geophysical applications. *Geophysical Research Letters* 25(21), 4035-4038.

[9] Chen, C. W. & Zebker, H. A. (2001). Two-dimensional phase unwrapping using statistical models for cost functions in nonlinear optimization. *Journal of the Optical Society of America A*, 18(2), 338-351.

[10] Otten, M. & Dow, J. (2005). *Envisat precise orbit determination*. In Proc. 2004 ENVISAT & ERS Symposium, Salzburg, Austria, 6-10 Sep 2004, ESA SP-572 (CD-ROM), ESA Publications Division, European Space Agency, Noordwijk, The Netherlands.